Draft version December 8, 2025
Typeset using LaTeX **twocolumn** style in AASTeX7.0.1

First Statistical Detection of Cool Gas Outflows with JWST Towards Cosmic Dawn

Chequiu Lyu [1,2,*] Haoran Yu [1,2,*] Enci Wang [1,2] Junxian Wang [1,2] Cheng Jia [1,2] Jie Song [1,2]
Yangyao Chen [3,4] Jinyang Wang,[1,2] Zeyu Chen [1,2] Chengyu Ma [1,2] Yifan Wang,[1,2] and Xu Kong [1,2]

[1] *Department of Astronomy, University of Science and Technology of China, Hefei, Anhui 230026, China*
[2] *School of Astronomy and Space Science, University of Science and Technology of China, Hefei, Anhui 230026, China*
[3] *School of Astronomy and Space Science, Nanjing University, Nanjing, Jiangsu 210093, China*
[4] *Key Laboratory of Modern Astronomy and Astrophysics, Nanjing University, Ministry of Education, Nanjing, Jiangsu 210093, China*

ABSTRACT

Galactic-scale outflows are a crucial component of galaxy evolution, yet their properties in the early universe remain poorly constrained. We present the first statistical investigation of cool gas outflows in galaxies spanning a wide cosmic timeline from $z \approx 1$ to $z \approx 10$. Using thousands of public JWST/NIRSpec spectra, we employ a signal-to-noise weighted spectral stacking technique on the Mg II $\lambda\lambda 2796, 2803$ absorption doublet. We robustly detect blueshifted Mg II absorption in all stellar mass and redshift bins. The outflow equivalent width exhibits a strong, positive correlation with stellar mass (M_*) at all epochs, increasing from ~ 1 Å at $M_* \approx 10^9$ $M_\odot$ to over 3 Å at $M_* > 10^{10.5}$ $M_\odot$. Our work provides the first statistical constraints on cool outflows in the low-mass ($M_* \lesssim 10^{9.5}$ $M_\odot$), high-redshift ($z > 3$) regime, vital for constraining feedback in the numerous progenitors of typical present-day galaxies. Crucially, the scaling relation between outflow properties and stellar mass shows no significant evolution at $z > 3$. This suggests a persistent, unevolving feedback mechanism governing the baryon cycle in the early universe, placing strong constraints on models that invoke a fundamental change in feedback physics at Cosmic Dawn, such as the feedback-free starburst model.

Keywords: Galaxies — CGM — Gas outflows — Absorption lines

1. INTRODUCTION

Galactic-scale outflows are fundamental to our understanding of galaxy evolution. Driven by energetic feedback from massive stars, supernovae (SNe), and active galactic nuclei (AGN) (e.g., J. Silk & M. J. Rees 1998; S. Veilleux et al. 2005; D. J. Croton et al. 2006; S. Veilleux et al. 2020), these outflows act as a key regulatory agent in the baryon cycle between galaxies and their surrounding environments. By expelling gas from the interstellar medium (ISM), they modulate the fuel available for star formation, thereby shaping the mass assembly of galaxies over cosmic time (e.g., T. Di Matteo et al. 2005; P. F. Hopkins et al. 2008; R. S. Somerville et al. 2008; D. K. Erb 2015). Furthermore, these outflows are the primary mechanism for transporting chemically enriched material from galaxies into the circumgalactic medium (CGM) and even the intergalactic medium (IGM), playing a crucial role in the cosmic metal enrichment history (e.g., M. Pettini et al. 2001; C. A. Tremonti et al. 2004; K. Finlator & R. Davé 2008; J. Tumlinson et al. 2017; E. Wang & S. J. Lilly 2021; Z. Chen et al. 2025a,b; C. Lyu et al. 2025a). Despite their acknowledged importance in theoretical models and hydrodynamical simulations of galaxy formation, establishing robust observational constraints on the physical properties of outflows remains a significant challenge, particularly in the early universe.

Observing outflows becomes progressively more difficult at high redshifts. During the peak epoch of cosmic star formation ($z \sim 1-3$), outflows are known to be ubiquitous in massive star-forming galaxies (e.g., B. J. Weiner et al. 2009; K. H. R. Rubin et al. 2014; N. M. Förster Schreiber et al. 2019). However, pushing these studies towards the epoch of Cosmic Dawn ($z > 6$) presents formidable challenges. The intrinsic faintness of high-redshift galaxies makes it extremely difficult to obtain spectra with sufficient signal-to-noise ratio (S/N) to detect the subtle absorption features imprinted by outflows on the galaxy's continuum. Consequently, most studies have been limited to either lensed systems or

Email: lyucq@ustc.edu.cn, ecwang16@ustc.edu.cn
* These authors contributed equally to this work.

the most luminous, rare objects (e.g. F. Valentino et al. 2025), hindering a comprehensive statistical analysis.

Absorption line spectroscopy is a powerful and widely used technique to probe the kinematics of cool gas flows along the line of sight. Blueshifted low-ionization metal absorption lines, such as the Mg II $\lambda\lambda2796, 2803$ doublet and the Na I D $\lambda\lambda5890, 5896$ doublet, are particularly effective tracers of cool ($T \sim 10^4$ K), neutral gas in outflows (e.g., B. J. Weiner et al. 2009; C. L. Martin et al. 2012; K. H. R. Rubin et al. 2014). The Mg II doublet, commonly detected in the CGM of galaxies, is a robust indicator of enriched cool gas over a wide range of H I column densities (J. Bergeron & G. Stasińska 1986; C. W. Churchill et al. 2000). The Na I D doublet, with its low ionization potential (5.1 eV), specifically traces dense, neutral regions often shielded by dust (B. D. Savage & K. R. Sembach 1996; D. Baron et al. 2020). However, due to their weakness, detecting these features in individual high-redshift galaxies is often infeasible.

The advent of the James Webb Space Telescope (JWST, J. P. Gardner et al. 2006) is revolutionizing the study of high-redshift galaxies. With its unprecedented sensitivity and near-infrared spectroscopic capabilities, JWST/NIRSpec provides high-quality spectra that are essential for outflow studies, free from the bright atmospheric sky background that hampers ground-based observations. This enables the detection of rest-frame optical features like Na I D at high redshifts for the first time (e.g., S. Belli et al. 2024; G. Cresci et al. 2023; R. L. Davies et al. 2024; E. Kehoe et al. 2025), and allows for the use of consistent rest-frame UV tracers like Mg II across a vast cosmic timeline ($z \sim 1-10$). The ability to assemble large spectroscopic samples of typical galaxies at these early epochs finally opens the door to characterizing the statistical properties of outflows and establishing crucial scaling relations that link outflow properties to intrinsic galaxy parameters, such as stellar mass and redshift.

JWST also opens a new frontier for testing galaxy formation theories in the early universe. Recently, new models have been proposed to explain the surprising abundance of luminous galaxies observed by JWST at $z \gtrsim 10$. One prominent example is the "feedback-free starburst" (FFB) model (A. Dekel et al. 2023; Z. Li et al. 2024). This model posits that at the high gas densities and low metallicities prevalent at Cosmic Dawn, the star formation timescale can become shorter than the delay time for stellar feedback from supernovae and stellar winds. This could lead to a highly efficient, bursty mode of star formation, fundamentally different from the self-regulating feedback processes observed at later cosmic times. The physical properties of galactic outflows—such as their velocities, equivalent widths, and scaling relations with galaxy properties—serve as direct probes of the underlying feedback mechanisms. By statistically characterizing outflows towards Cosmic Dawn, we can test the predictions of models like the FFB and determine whether a shift in the nature of feedback indeed occurred in the early universe.

In this work, we leverage the vast public dataset from the DAWN JWST Archive (DJA) to conduct the statistical investigation of cool gas outflows in galaxies spanning the redshift range $1 < z < 10$. By employing a spectral stacking technique on hundreds of JWST/NIRSpec spectra, we significantly enhance the S/N, enabling the detection of the faint, average outflow signals that are invisible in individual spectra. The primary goals of this Letter are: (1) to reliably detect outflow traced by Mg II and Na I D at different redshift, and measure the average outflow velocities and equivalent widths (EW) traced by Mg II across a range of redshifts and stellar masses; and (2) to quantitatively establish the scaling relations between outflow properties, galaxy stellar mass, and cosmic time; and (3) to provide key observational constraints on the physics of galactic feedback and its role in galaxy evolution towards the Cosmic Dawn.

This Letter is structured as follows. In Section 2, we describe our data and sample selection. In Section 3, we detail our methodology for spectral stacking and measuring outflow properties. We present our main results and discussion in Section 4. Finally, we summarize our findings in Section 5. Throughout this Letter, we adopt a ΛCDM cosmology with $H_0 = 70$ km s^{-1} Mpc^{-1}, $\Omega_m = 0.3$, and $\Omega_\Lambda = 0.7$, and assume a G. Chabrier (2003) stellar initial mass function (IMF).

2. DATA AND SAMPLE SELECTION

Our analysis is based on the JWST/NIRSpec spectra dataset from the DAWN JWST Archive (DJA)[5]. Specifically, we utilize the v4.4 Merged Table [6] and its associated extended spectra catalog (F. Valentino et al. 2025; C. L. Pollock et al. 2025). This comprehensive public catalog provides 80,367 uniformly processed spectra, reduced using the `msaexp` (G. Brammer 2022; A. de Graaff et al. 2025; K. E. Heintz et al. 2025) and `grizli` (G. Brammer 2023) pipelines. The data products include 1D/2D spectral extractions, redshift measurements, emission-line fluxes, and associated

[5] https://dawn-cph.github.io/dja/

[6] https://dawn-cph.github.io/dja/blog/2025/05/01/nirspec-merged-table-v4/

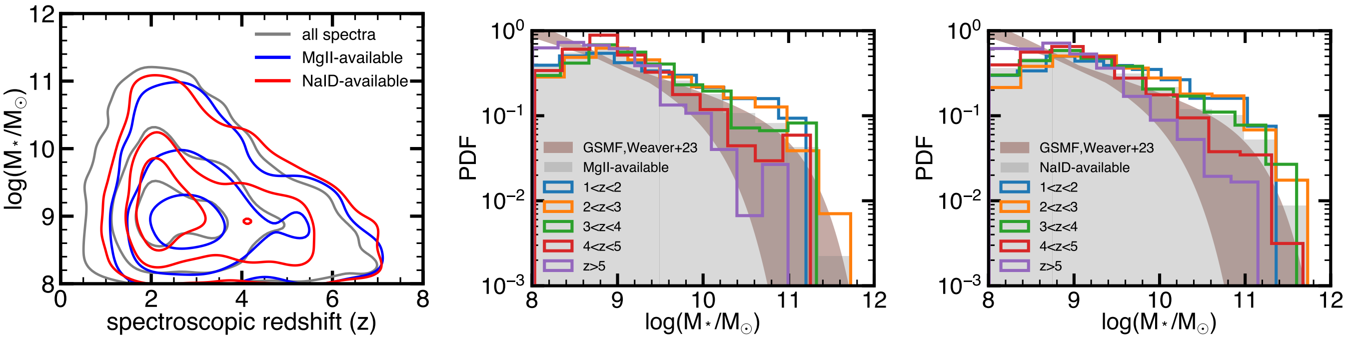

Figure 1. Sample selection and stellar mass distribution. The left panel displays the distribution of our galaxy samples in the stellar mass-redshift plane. The grey contours represent the parent sample of 24,927 galaxies, while the blue and red contours show the subsamples with valid spectral coverage of the Mg II and Na I D doublets, respectively. The three contour levels for each sample are derived from a Kernel Density Estimate (KDE) and correspond to the 16th, 50th, and 84th percentiles of the distribution. The middle and right panels present the Probability Density Functions (PDFs) of the stellar mass distributions for the Mg II- and Na I D-available subsamples. The colored histograms correspond to the different redshift bins as labeled. To assess the representativeness of our sample, we overlay the evolving Galaxy Stellar Mass Function (GSMF) from J. R. Weaver et al. (2023). The brown shaded region represents the envelope of the GSMF across the redshift range $1.1 < z < 7.5$, derived from the Schechter function parameters (double for $z < 3$ and single for $z > 3$) presented in their work. The close agreement in shape demonstrates that our sample is broadly representative of the underlying galaxy population at these epochs.

photometry. The complete dataset is available at DOI: 10.5281/zenodo.1547235.

We construct our parent sample by selecting galaxies with a photometrically derived stellar mass (M_*) greater than $10^8\ M_\odot$ and a secure spectroscopic redshift. The redshift quality is assessed via visual inspection flags provided in the catalog. We exclude spectra with poor quality flags, specifically `Grade`$= 0$ (spectrum suffers some data quality issue) and `Grade`$=-1$ (fit not performed or graded). This initial selection results in a sample of 24,927 galaxy spectra.

To search for cool gas outflows, we create subsamples based on the spectral coverage of the Mg II $\lambda\lambda2796, 2803$ and Na I D $\lambda\lambda5890, 5896$ doublets. We select objects observed with NIRSpec medium- or high-resolution grisms (G140M/H, G235M/H, G395M/H; $R \sim 1000/2700$) that provide unmasked spectral coverage of a 100 Å window roughly centered on these doublets (i.e., 2750–2850 Å for Mg II and 5850–5950 Å for Na I D). This selection ensures that the absorption features, if present, fall within the observed spectral range and are sampled at a sufficient resolution for detection. This procedure yields final samples of approximately 2,394 spectra for the Mg II analysis and 5,512 spectra for the Na I D analysis. However, due to the emission line blending and inherent stellar contamination, we do not investigate the scaling relations with galaxy properties of Na I D sample in this work (See Section 4.1 for details).

The properties and representativeness of our final samples are summarized in Figure 1. The left panel shows the coverage of our parent sample and the Mg II- and Na I D-available subsamples across the stellar mass-redshift plane. The middle and right panels show the normalized stellar mass distributions (as PDFs) for our subsamples, binned by redshift.

To investigate whether our sample is a representative galaxy sample, we compare our distributions to the evolving Galaxy Stellar Mass Function (GSMF) from the comprehensive JWST analysis of J. R. Weaver et al. (2023). Although our sample is from a wide range of programs and surveys for different propose, as shown by the brown shaded envelope in Figure 1, which encapsulates the GSMF evolution from $z = 1.1$ to $z = 7.5$, our sample distributions trace the shape of the underlying galaxy population remarkably well, particularly at the high-mass end ($M_* > 10^9 M_\odot$) where the majority of the cosmic stellar mass resides. This agreement confirms that our spectroscopic sample is broadly representative of the typical galaxy population across the full mass and redshift range of our study. Therefore, the outflow properties derived in this work are characteristic of the general galaxy population during these cosmic epochs.

3. SPECTRA STACKING METHOD

To systematically investigate the prevalence of galactic outflows across the galaxy population, we stack galaxy spectra binned by their physical properties. This technique significantly improves S/N, enabling the detection of outflow signatures that are too faint to identify in individual spectra (e.g. B. J. Weiner et al. 2009; Y.-M. Chen et al. 2010; K. H. R. Rubin et al. 2010; R. Bordoloi et al. 2014).

3.1. *Weighted Median Stacking*

We begin by shifting all individual spectra to their rest-frame. For each spectrum, we extract the spectral data within a 200Å window centered on the doublet features (2700–2900Å for Mg II and (5800–6000Å for Na I D) . These segments are then resampled onto a unified wavelength grid using `Spectres` (A. C. Carnall 2017). To avoid artificial super-sampling, which could introduce additional errors, the wavelength interval for the resampled spectra is inferred from the sample redshift, resulting in adopted intervals of $\Delta\lambda = 1.4$ Å$, 0.9$ Å$, 0.7$ Å$, 0.6$ Å$, 0.5$ Å for $1 < z < 2$, $2 < z < 3$, $3 < z < 4$, $4 < z < 5$ and $5 < z < 10$ bins, respectively. After masking the prominent lines (Mg II, Mg I, Na I D), we estimate the continuum by first applying a median filter with an 11-pixel window and then fitting a 5th-order polynomial to the smoothed spectrum. Each original spectrum is divided by its corresponding continuum to produce a normalized spectrum. In idealized circumstances, the normalized flux should be unity across non-absorbing regions. However, the normalization can be biased in cases of low S/N or unexpected strong absorption features, thereby introducing additional uncertainty into the stacked spectrum. For instance, if the fitted continuum approaches or crosses zero, the normalized flux can diverge, producing a singularity.

Aiming at minimizing the impact of poorly constrained normalizations to the spectra stacking processes, we define a weight, w, to evaluate the reliability of the spectra normalization. It is defined as

$$w \equiv \frac{1}{\sum_{i=1}^{N}(F_i - F_i^{\rm ref})^2/N}, \tag{1}$$

where F_i is the ith flux density in the normalized spectrum, $F_i^{\rm ref} = 1$ is the reference value for a perfectly normalized spectrum, and N is the quantity of the spectral data points. In this calculation, the regions with expected spectral lines (Mg II, Mg I, Na I D) are masked. We then generate the median-stacked spectra based on these weights. The composite flux in each wavelength bin is computed as the weighted median of all individual fluxes. For n ordered fluxes $f_1, f_2, \cdots, f_n$ with corresponding weights $w_1, w_2, \cdots, w_n$, the weighted median is defined as the element f_k satisfying

$$\frac{\sum_{i=1}^{k-1} w_i}{\sum_{i=1}^{n} w_i} \le \frac{1}{2} \quad \text{and} \quad \frac{\sum_{i=k+1}^{n} w_i}{\sum_{i=1}^{n} w_i} \le \frac{1}{2}. \tag{2}$$

In such a regime, the impact of the spectra with poor normalization is minimized, because their weights are extremely small. Spectra of this kind occupy approximately 50% of the sample. Furthermore, to prevent a small fraction of spectra with high weights dominating the stack, we impose an upper threshold $w^{\rm thr}$, thereby

$$w = \begin{cases} w, & \text{if } w < w^{\rm thr}, \\ w^{\rm thr}, & \text{otherwise.} \end{cases} \tag{3}$$

Based on inspection of the weight distribution, we adopt $w^{\rm thr} = 1$ to mitigate the potential bias from the high-weight tail, and this threshold is employed throughout our study.

To quantify the uncertainty in the final stacked spectra, we employ a bootstrap resampling procedure. Specifically, we generate 1000 bootstrap samples, each by randomly drawing N spectra from the original set of N with replacement. For comparison, we have also performed an unweighted stacking analysis with equal probabilities; the results are presented in the Appendix A.

When determining the representative z, M_* of a bin, we employ the same weighting method, e.g., $\langle z \rangle_w$ is derived as the weighted median redshift using exactly the same weights derived from Equation 1, 2 and 3.

3.2. *Outflow Properties*

We employ the `boxcar` method (K. H. R. Rubin et al. 2010; R. Bordoloi et al. 2014) to derive the mean outflow velocity ($v_{\rm out}$) and the outflow equivalent width (EW$_{\rm out}$) of the Mg II doublet. This approach provides model-independent measurements directly from the observed absorption profile, which is advantageous for our statistical analysis. Given the blending between the red-wing of Mg II λ2796 line and the blueshifted Mg II λ2803 absorption, we use the blue-wing of Mg II λ2796 and the red-wing of Mg II λ2803 to trace the kinematics of the species. We conceptually decompose the absorption into a blueshifted outflowing component (denoted as "out") characterized by a blueshifted line center, and an interstellar component (denoted as "sym") with a symmetrical profile centered at the rest-frame wavelength. The EWs are measured in two velocity intervals: EW$_{\rm blue}$ from -700 to 0 km s^{-1} relative to Mg II λ2796, and EW$_{\rm red}$ from 0 to +400 km s^{-1} relative to Mg II λ2803, which are defined empirically to cover the extended absorption wings. Following R. Bordoloi et al. (2014), the total absorption EW, defined as $\mathrm{EW_{tot}} \equiv \mathrm{EW_{out}} + \mathrm{EW_{sym}}$, and the outflow EW are estimated as

$$\begin{aligned} \mathrm{EW_{tot}} &= 2(\mathrm{EW_{blue}} + \mathrm{EW_{red}}), \\ \mathrm{EW_{out}} &= 2(\mathrm{EW_{blue}} - \mathrm{EW_{red}}). \end{aligned} \tag{4}$$

The EW-weighted mean velocity of the total absorption profile can be calculated as $v_{\rm tot}$. Assuming the symmetrical component is centered at zero velocity, the mean outflow velocity is given by

$$v_{\rm out} = \frac{\rm EW_{tot}}{\rm EW_{out}} \cdot v_{\rm tot}. \qquad (5)$$

The uncertainties in $\rm EW_{out}$ and $v_{\rm out}$ are estimated from our bootstrap analysis. We apply the aforementioned `boxcar` measurement to each of the 1000 bootstrap spectra, thereby generating distributions of $\rm EW_{out}$ and $v_{\rm out}$. The 1σ uncertainty for each parameter is then quoted as the standard deviation of its respective distribution.

The `boxcar` method, while model-independent, can yield non-physical results under specific conditions. In the typical observed outflows, one expects $\rm EW_{out} > 0$ and $v_{\rm out} < 0$. However, in the presence of significant noise or complex kinematics, the method may produce $\rm EW_{out} < 0$ or $v_{\rm out} > 0$. We note that $\rm EW_{out} < 0$ indicates more absorption in the red wing, which is suggestive of inflow features. However, this method tailored for outflow characterization is not suitable for the corresponding analysis. When $\rm EW_{out}$ is small, the derived $v_{\rm out}$ becomes unstable to and may diverge to spuriously large values, which should be treated with caution.

To validate the robustness of our stacking analysis, we also implement the same `boxcar` measurement on individual galaxy spectra. First we identify potential outflow candidates by conducting a visual inspection of all JWST spectra which covers Mg II region, selecting those with discernible Mg II absorption features. For these candidates, we calculate the Mg II absorption EW by integrating the absorbed flux between 2790 Å and 2808 Å. The uncertainty in the EW, EW_err, is derived from the error of the flux densities. We then apply a S/N cut of EW_err > 5, which yields a final sample of 42 individual JWST spectra with significant Mg II absorption. The properties and spectra of these sources are tabulated and presented in the Appendix B.

4. RESULTS AND DISCUSSION

4.1. *Absorption Feature Across Cosmic Time*

Figure 2 shows the final stacked spectra for five distinct redshift bins. Our S/N-weighted stacking technique successfully reveals clear absorption features for both the Mg II and Na I D doublets across the cosmic timeline probed by our sample ($1 < z < 10$). Despite showing greater spectral fluctuations, the stacked spectra produced using equal-weight stacking also exhibit consistent blueshifted absorption features (see left panels of Figure 7). This consistency confirms that the detected outflow signal is robust and not an artifact of our weighting scheme. The left panels reveal consistently blueshifted absorption troughs relative to the systemic velocities (marked by the red dashed lines), providing clear evidence for the prevalent cool outflows. The S/N of the composite spectra varies across redshift bins, a difference primarily attributed to the number and intrinsic quality of the spectra contributing to each stack. We note that here we focus on establishing the detection of these blueshifted outflows across cosmic time. A robust quantification of their evolutionary trend is not feasible with the current dataset, as the underlying distributions of key galaxy properties (e.g., mass, star formation rate) differ between redshift bins.

The Na I D doublet, shown in the right panels, is also detected in the stacked spectra, showing blueshifted absorption features. However, as shown in Figure 2, the blue wing of the absorption is blended with the strong He I λ5876 emission line, hindering local continuum subtraction. Furthermore, the Na I D absorption is less prominent than Mg II.

More fundamentally, the observed Na I D absorption is a composite signal. It originates not only from cool, neutral gas in the ISM—the component tracing the outflow—but also from the stellar photospheres within the host galaxy's stellar population. This stellar absorption component arises predominantly from the atmospheres of cool, evolved stars (e.g., K and M giants and supergiants), which can contribute substantially to the total observed EW (e.g., T. M. Heckman et al. 2000; D. S. Rupke et al. 2005). Disentangling the ISM contribution from this stellar contamination is highly non-trivial and requires sophisticated full spectral fitting with stellar population synthesis (SPS) models. Such modeling is fraught with uncertainties, especially for high-redshift galaxies where the stellar populations are less well-constrained.

Given these combined challenges of emission line blending and inherent stellar contamination, a robust measurement of the ISM outflow properties from the Na I D doublet would be highly model-dependent and subject to large systematic uncertainties. Therefore, we focus our subsequent detailed analysis exclusively on the Mg II doublet as a cleaner tracer of the cool gas outflows. We do not perform further analysis of the Na I D feature in stellar mass bins or investigate its potential scaling relations with galaxy properties in this work.

4.2. *Absorption Feature Across Stellar Mass Bins*

To explore the dependence of outflow properties on host galaxies, we subdivide our sample into stellar mass bins within each redshift interval. The stellar mass binning is designed to optimize the trade-off between the number of spectra and the S/N ratio, ensuring a robust detection in each bin. The stacked Mg II absorption features for these bins are presented in Figure 3. We

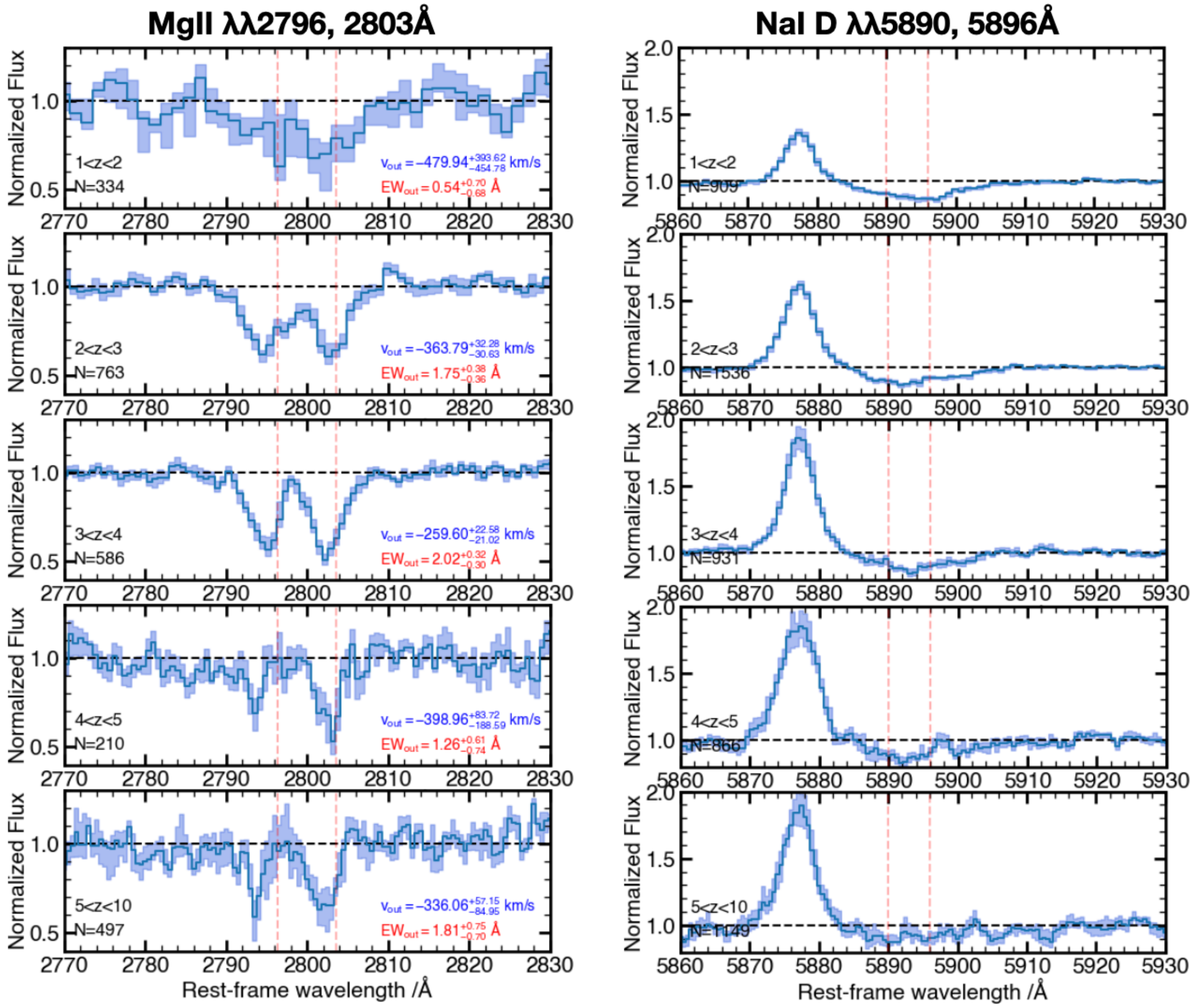

Figure 2. Stacked absorption feature in redshift bins. The left and right columns show the continuum-normalized stacked spectra centered on the Mg II $\lambda\lambda2796, 2803$ and Na I D $\lambda\lambda5890, 5896$ doublets, respectively. Each row corresponds to a different redshift bin, as indicated in the bottom-left corner of each panel. The blue solid line represents the weighted median spectrum, while the shaded region shows the 1σ uncertainty derived from bootstrap resampling. The horizontal dashed line is the continuum level at unity, and the vertical red dashed lines mark the rest-frame wavelengths of the doublet components. The number of spectra in each stack (N) and the derived outflow velocity and EW are also annotated.

find that low-mass bins require a larger number of constituent spectra to achieve a S/N comparable to that of high-mass bins, which could be the result of the relatively low S/N for low-mass galaxy individual spectra. Blueshifted absorption troughs are detected across all mass bins, confirming the prevalence of cool gas outflows in galaxies of diverse masses.

However, the outflow signal in the $1 < z < 2$ bins is notably not significant, yielding small $\mathrm{EW}_{\mathrm{out}}$ values and unstable, spuriously large v_{out} values. This is likely attributable to the limited sample size and the low spectral S/N of JWST galaxies with Mg II coverage in this redshift range, despite previous studies having robustly detected outflows at similar epochs (B. J. Weiner et al. 2009; R. Bordoloi et al. 2014; H. Yu et al. in prep.). In contrast, the $2 < z < 3$ and $3 < z < 4$ bins exhibit high S/N composite spectra, enabling well-constrained measurements of $\mathrm{EW}_{\mathrm{out}}$ and v_{out} suitable for statistical analysis. For the highest redshift bins ($4 < z < 5$ and $5 < z < 10$), the absorption profiles, though noisy, display clear blueshifts. This provides strong evidence that cool gas outflows are already present at $z > 5$ (corresponding ~ 1 Gyr of the Universe) galaxies. To our knowledge, this is the first statistical detection of outflow signatures in $z > 3$ galaxies, indicating that feedback mechanisms plays a critical role in the early phase of galaxy evolution.

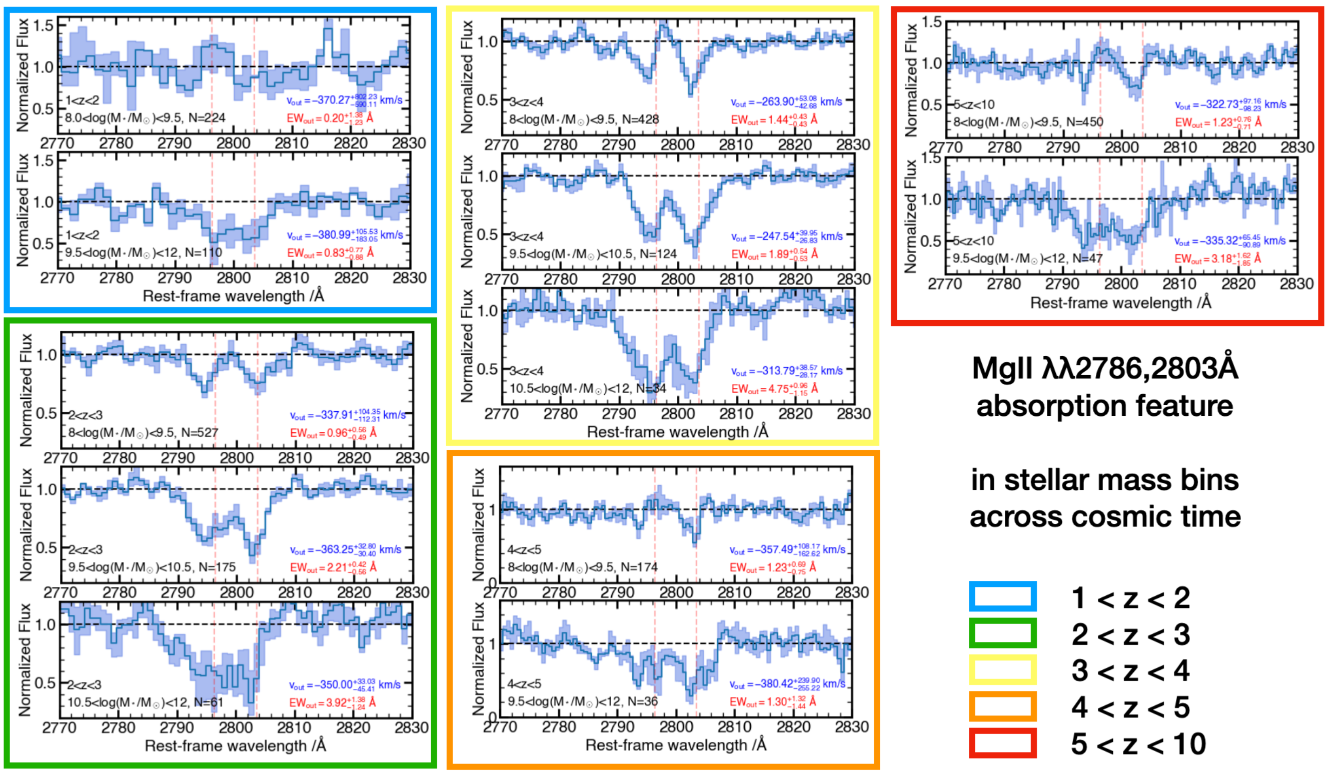

Figure 3. Stacked Mg II feature in stellar mass and redshift bins. Each colored box corresponds to a specific redshift bin, as indicated by the legend on the right. Within each box, the panels are arranged in order of increasing stellar mass from top to bottom. The stellar mass range and the number of spectra (N) in each stack are annotated in each panel. The blue solid line, shaded uncertainty region, and dashed lines are the same as in Figure 2.

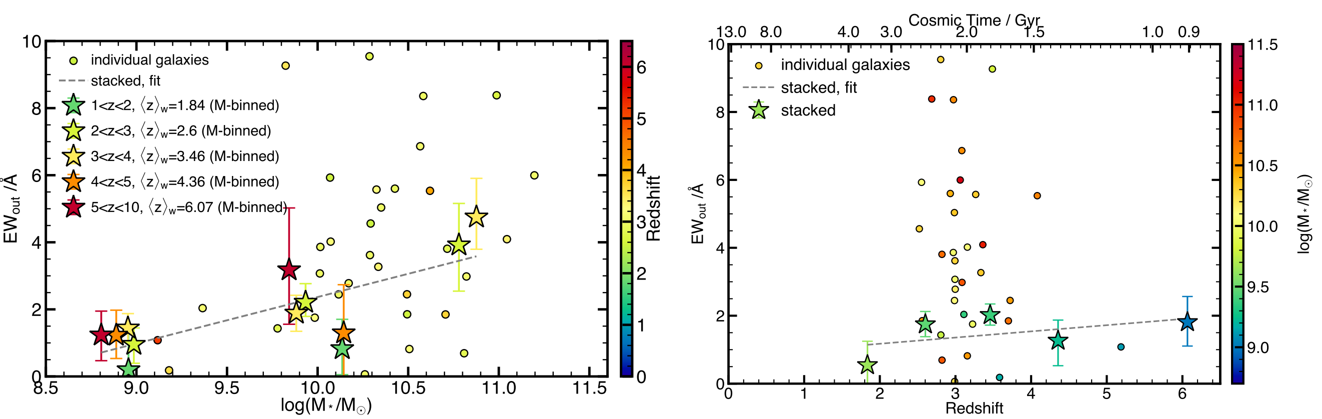

Figure 4. Scaling relations for the Mg II absorption EW. **Left panel:** The outflow EW as a function of stellar mass. Our stacked measurements are shown as star symbols, color-coded by their weighted mean redshift. The grey dashed line shows a linear fit to the stacked data points. For comparison, small circles show the measurements from the individual galaxies presented in the Appendix B, color-coded by their redshift. **Right panel:** The outflow EW as a function of redshift, with an additional top axis showing cosmic time. The star symbols again represent our stacked results, but all data points are now color-coded by their weighted mean stellar mass, as indicated by the colorbar. The grey dashed line is a linear fit to the stacked data.

4.3. *Scaling Relations of Outflow Properties*

The scaling relations for the measured Mg II EW_{out} are displayed in Figure 4. Our stacked measurements (star symbols) demonstrate that EW_{out} systematically increases with stellar mass across all cosmic epochs. A linear fit to the stacked data (grey dashed line) confirms this dominant trend, and we find no significant offset for the high-redshift stacks, indicating that galaxies from all

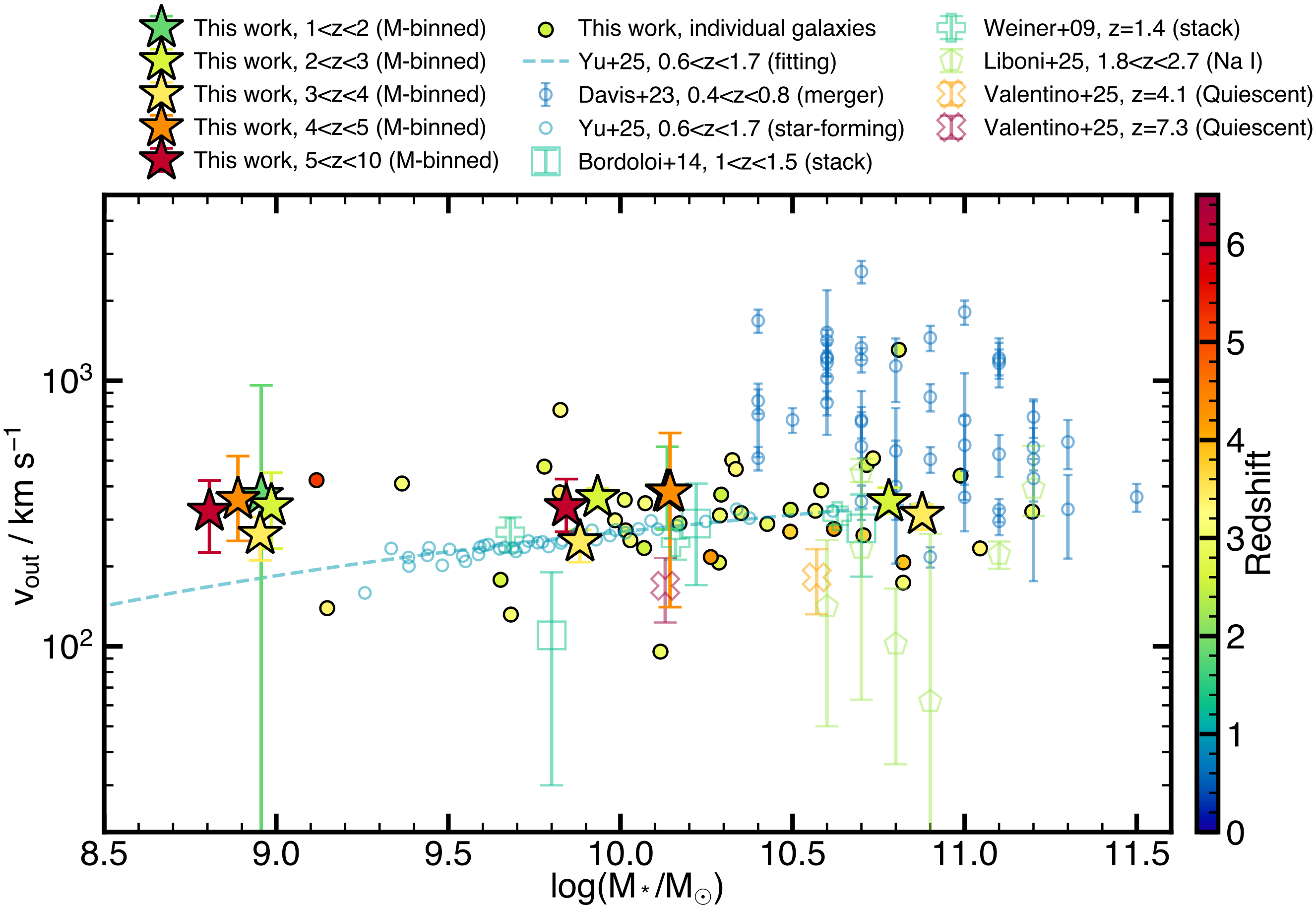

Figure 5. The outflow velocity versus stellar mass relation. Our measurements from the weighted stacking are shown as star symbols. The color of our data points corresponds to the mean redshift of the stack, as indicated by the color bar on the right. We compare our results with literature data from B. J. Weiner et al. (2009), R. Bordoloi et al. (2014), J. D. Davis et al. (2023), H. Yu et al. (in prep.), C. Liboni et al. (2025), and F. Valentino et al. (2025), as detailed in the legend. Our work provides new constraints, particularly at the low-mass, high-redshift ($z > 3$) end of the parameter space.

epochs broadly follow a universal mass-EW_{out} relation. For comparison, we also plot individual detections from our gallery in Appendix B (small circles), which, despite exhibiting significant scatter at a fixed mass, follow the same average trend. These sources systematically exhibit larger EW_{out} than the stacked results, indicating that selection effects plays a role in analyzing individual detections.

The right panel of Figure 4 shows the outflow EW as a function of redshift. No simple, monotonic trend with cosmic time is detected, which is primarily a consequence of the strong mass-dependence of the EW, combined with the fact that the average stellar mass of our stacked samples evolves with redshift (as visualized by the color-coding of the star symbols). For instance, the stacked point at $z \sim 6$ has a lower EW than the point at $z \sim 3$, not necessarily because outflows are intrinsically weaker, but because the average mass of the $z \sim 6$ stack is significantly lower. Taken together, these two panels strongly indicate that stellar mass of galaxies is linked to the cool gas outflow EW.

A comparison between our measured outflow velocities and a compilation of literature results is presented in Figure 5. Our measurements (star symbols) significantly extend previous works into the low-mass, high-redshift frontier. A key result from this comparison is the remarkable consistency of outflow velocities at $z > 3$. Across our redshift bins from $z \sim 3$ up to $z \sim 10$, the outflow velocities remain robustly centered around $\sim 350\,\mathrm{km\,s^{-1}}$ and do not exhibit significant evolution. This lack of evolution at high redshifts is a primary finding of our work.

For context, cool outflow velocities in the literature vary with galaxy properties. For instance, vigorous starbursts in merging galaxies can drive outflows up to $\sim 1000\,\mathrm{km\,s^{-1}}$ (J. D. Davis et al. 2023), whereas quiescent galaxies exhibit slower winds (F. Valentino et al. 2025). Our results for typical star-forming galaxies at

$z > 3$ establish a crucial baseline in a previously unexplored regime. While there might be an evolution in outflow properties from $z < 2$ to $z > 2$, our data robustly show that for $z > 3$, the relationship between outflow velocity and stellar mass is largely unevolving.

Furthermore, we find that the cool outflow velocities in the literature varies with the properties of galaxies. For instance, vigorous starbursts in merging galaxies can drive outflows up to ~ 1000 km, s^{-1} (J. D. Davis et al. 2023), whereas quiescent galaxies exhibit slower winds (F. Valentino et al. 2025). The mean outflow velocity measured from our individual spectra (mostly at $3 < z < 4$) are consistent with the scaling relation of H. Yu et al. (in prep.), which was established using low-redshift star-forming main sequence (SFMS) galaxies. Nonetheless, our stacked results yield systematically higher velocities, particularly at the low-mass end. Although we have claimed that the measurement in the low-mass bin of $1 < z < 2$ sample could be affected by numerical instability, the elevated velocities in higher-redshift low-mass bins appear robust. This indicates that the high-redshift JWST galaxies in our study may be experiencing more intense, bursty star formation, potentially driving stronger outflows (T. J. Looser et al. 2025; L. Clarke et al. 2025; C. Lyu et al. 2025b). This also suggests that the dynamics of the cool gas outflows before the cosmic noon may differ fundamentally from those in the low-redshift universe.

Crucially, thanks to the large and deep JWST sample, we provide statistical constraints on the velocities of cool gas outflows in low-mass ($M_* \lesssim 10^{9.5}$ $\mathrm{M}_\odot$) galaxies at $z > 3$. These measurements in the low-mass, high-redshift regime are vital for constraining feedback models, as they probe the numerous progenitors of today's typical galaxies during their most active growth phases. While there is some evidence for an evolution in the $v_{\rm out} - M_*$ relation from $z < 1$ (literature) to $z \approx 2$, we find no significant further evolution at higher redshifts ($z > 3$).

Figure 6 presents another view of our results, showing the outflow velocity as a function of cosmic time. At first glance, the evolution of our measured outflow velocities (star symbols) with redshift appears complex, with no simple monotonic trend. However, this is primarily a consequence of selection effects, as the mean stellar mass of our stacked samples generally decreases with increasing redshift, which is clearly visualized by the color-coding of the data points. This figure starkly illustrates the unique contribution of our work: providing the statistically-derived outflow velocity measurements for typical star-forming galaxies at $z > 3$ and on the approach to the Cosmic Dawn.

Combining the results from Figures 4, 5, and 6, This lack of significant evolution in the outflow properties at $z > 3$ provides a powerful test for theoretical models of galaxy feedback in the early universe. For instance, the feedback-free starburst (FFB) model (A. Dekel et al. 2023; Z. Li et al. 2024) predicts a fundamental transition in the mode of star formation for massive galaxies at $z \gtrsim 8 - 10$, where feedback is posited to become inefficient. Such a dramatic change in the interplay between star formation and feedback would presumably lead to a significant alteration in outflow properties, or perhaps even a suppression of the strong, organized outflows that we observe. Contrary to this prediction, our findings reveal a remarkable consistency in outflow properties from $z \sim 3$ up to $z \sim 10$. The fact that galaxies at $z > 5$ follow similar scaling relations and exhibit similar outflow velocities to those at $z \sim 3 - 4$ suggests a persistent, unevolving feedback mechanism is already in place by $z = 10$. This result challenges the scenario where the FFB mechanism is the dominant mode governing the baryon cycle in the typical star-forming galaxies probed by our sample, placing a strong constraint on its applicability.

The quantitative measurements of the outflow properties derived from our stacked spectra, including the number of galaxies, weighted-mean redshift and stellar mass, outflow velocities, and EWs for each bin, are fully tabulated in Table 1.

4.4. *Synergy of Stacking and Individual Analysis*

A key strength of our work is the synergistic combination of a statistical stacking analysis with a targeted study of individual detections. As Figure 8 in Appendix B illustrates, the galaxies with the most prominent, high-S/N absorption features are typically massive ($M_* > 10^{10}$ $\mathrm{M}_\odot$). These individual detections serve as unambiguous proof-of-concept, confirming the physical reality of the outflow phenomenon and revealing the rich diversity of absorption profile morphologies. This diversity includes not only powerful outflows but also a few intriguing cases of redshifted absorption as potential signatures of gas accretion (inflow), which we defer to a future, more detailed analysis (see Appendix B).

However, these massive objects represent only a fraction of our full sample. The vast majority of galaxies, particularly at lower stellar masses ($M_* < 10^{9.5}$ $\mathrm{M}_\odot$), are numerous but have spectra with insufficient S/N for individual analysis. Thanks to the S/N-weighted stacking technique, we can unlock the statistical power of this dominant population, recovering the faint, average outflow signatures that are otherwise invisible. By bridging these two regimes, our approach provides the most com-

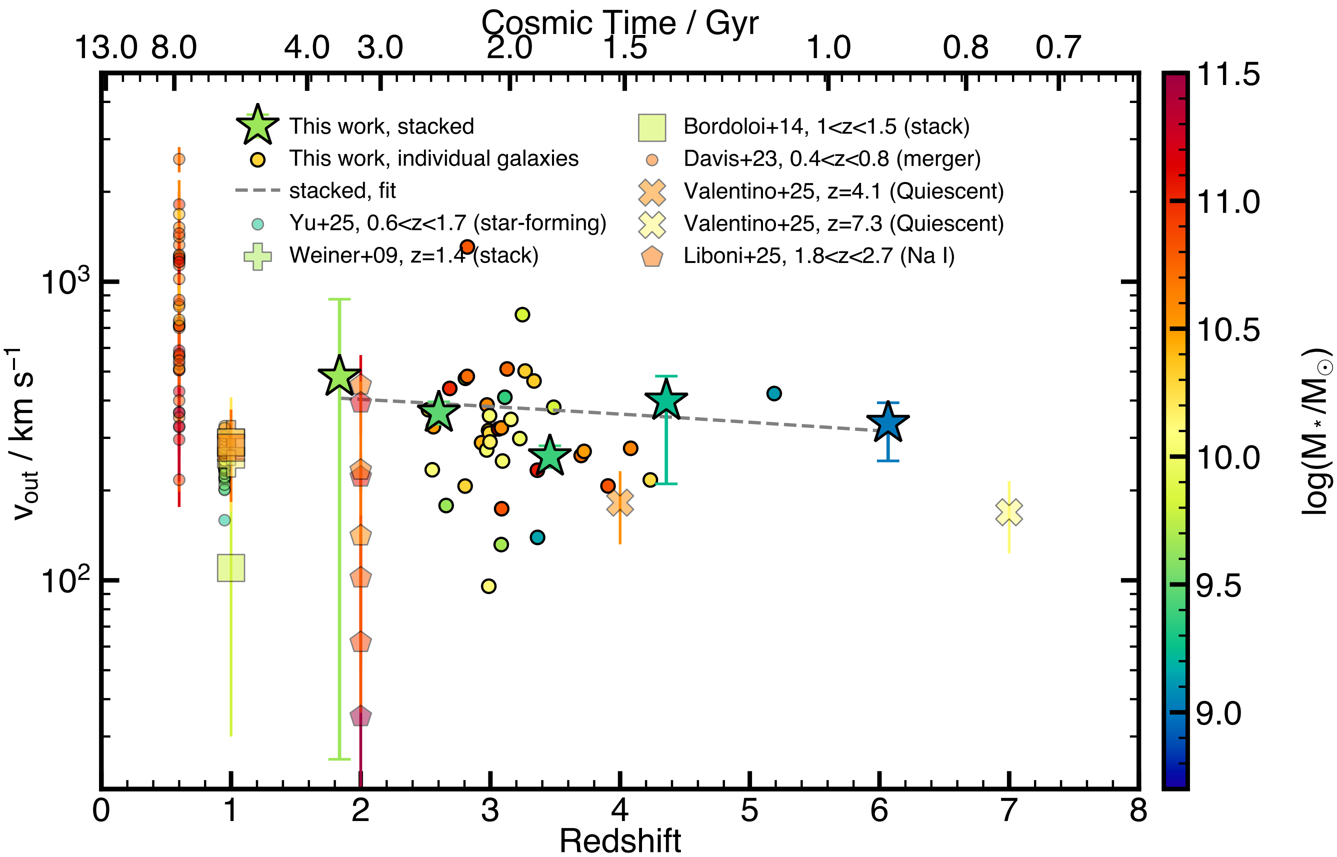

Figure 6. The cosmic evolution of outflow velocity. Our measurements from the full redshift bins stacks are shown as large star symbols. The color of all data points corresponds to the weighted mean stellar mass of the respective galaxy sample, as indicated by the color bar on the right. For context, we compare our results with a compilation of literature data from B. J. Weiner et al. (2009), R. Bordoloi et al. (2014), J. D. Davis et al. (2023), H. Yu et al. (in prep.), C. Liboni et al. (2025), and F. Valentino et al. (2025).

prehensive view possible, leveraging every spectrum to its full potential and robustly characterizing the properties of galactic outflows across the full dynamic range of our sample.

5. SUMMARY

We present the first statistical study of cool gas outflows in galaxies spanning a wide cosmic timeline from $z \approx 1$ to $z \approx 10$. Leveraging thousands of public JWST/NIRSpec spectra, we employ a S/N-weighted spectral stacking technique, complemented by an analysis of individual high-S/N detections, to robustly characterize the faint absorption signatures of the Mg II doublet. Our sample is shown to be broadly representative of the underlying galaxy population. Our main findings, derived from this powerful combined approach, are summarized as follows:

1. We robustly detect blueshifted Mg II absorption, indicative of cool galactic outflows, in all redshift and stellar mass bins across our entire sample range ($1 < z < 10$). The typical outflow velocities are substantial (~ 350 km s^{-1}), demonstrating that powerful outflows are a persistent feature of galaxy evolution. This work presents the first statistical detection of cool gas outflows in galaxies at $z > 3$.

2. The properties of cool gas outflows are linked to stellar mass of the host galaxy. We find a strong, positive correlation where the outflow equivalent width ($\mathrm{EW_{out}}$) systematically increases with stellar mass at all cosmic epochs. This suggests strong absorption from extensive outflowing reservoirs in high-mass galaxies.

3. Our work provides the first statistical constraints on cool gas outflows in the low-mass ($M_* \lesssim 10^{9.5}$ M$_\odot$), high-redshift ($z > 3$) regime. These measurements provide a crucial baseline for feedback models in the numerous progenitors of typical present-day galaxies.

Table 1. Properties of Stacked Samples and Outflow Measurements. The columns are as follows: (1) Redshift bin. (2) Weighted mean redshift of the bin. (3) Stellar mass bin. For rows with a dash, measurements correspond to the entire redshift bin. (4) Weighted mean of the logarithm of the stellar mass. (5) Number of spectra in the stack. (6) Weighted mean outflow velocity derived from the Mg II doublet. (7) Outflow equivalent width of the Mg II doublet.

z	$\langle z \rangle_w$	$\log M_*$ ($M_\odot$)	$\langle \log M_* \rangle_w$ ($M_\odot$)	N	$v_{\rm out}$ (km s^{-1})	EW$_{\rm out}$ (Å)
1–2	1.836	–	9.65	334	480^{+394}_{-455}	$0.54^{+0.70}_{-0.68}$
1–2	1.828	8.0–9.5	8.96	224	370^{+802}_{-590}	$0.20^{+1.38}_{-1.23}$
1–2	1.842	9.5–12.0	10.14	110	381^{+106}_{-183}	$0.83^{+0.77}_{-0.88}$
2–3	2.602	–	9.47	763	364^{+32}_{-31}	$1.75^{+0.38}_{-0.36}$
2–3	2.608	8.0–9.5	8.99	527	338^{+104}_{-112}	$0.96^{+0.56}_{-0.49}$
2–3	2.582	9.5–10.5	9.93	175	363^{+33}_{-30}	$2.21^{+0.42}_{-0.56}$
2–3	2.648	10.5–12.0	10.78	61	350^{+33}_{-45}	$3.92^{+1.38}_{-1.24}$
3–4	3.458	–	9.39	586	260^{+23}_{-21}	$2.02^{+0.32}_{-0.30}$
3–4	3.486	8.0–9.5	8.95	428	264^{+53}_{-43}	$1.44^{+0.43}_{-0.43}$
3–4	3.410	9.5–10.5	9.88	124	248^{+40}_{-27}	$1.89^{+0.54}_{-0.53}$
3–4	3.423	10.5–12.0	10.88	34	314^{+39}_{-28}	$4.75^{+0.96}_{-1.15}$
4–5	4.356	–	9.24	210	399^{+84}_{-189}	$1.26^{+0.61}_{-0.74}$
4–5	4.385	8.0–9.5	8.89	174	357^{+108}_{-163}	$1.23^{+0.69}_{-0.75}$
4–5	4.281	9.5–12.0	10.14	36	380^{+240}_{-255}	$1.30^{+1.32}_{-1.44}$
5–10	6.067	–	9.01	497	336^{+57}_{-85}	$1.81^{+0.75}_{-0.70}$
5–10	6.078	8.0–9.5	8.81	450	323^{+97}_{-98}	$1.23^{+0.76}_{-0.71}$
5–10	6.017	9.5–12.0	9.84	47	335^{+65}_{-91}	$3.18^{+1.62}_{-1.85}$

Note—The quoted uncertainties on $v_{\rm out}$ and EW represent the 1σ confidence intervals derived from 1000 bootstrap resampling iterations. The outflow properties are measured using the `boxcar` method described in Section 3.

4. There is no significant evolution in the cool gas outflow properties at high redshifts ($z > 3$). Both the scaling relation between outflow equivalent width and stellar mass, and the outflow velocities themselves, are remarkably consistent from $z \approx 3$ to $z \approx 10$. This suggests that a persistent, unevolving feedback mechanism is already governing the baryon cycle. This finding challenges theoretical models that predict a fundamental change or breakdown of feedback at Cosmic Dawn, such as the feedback-free starburst model, indicating it is likely not the dominant feedback process in the observed galaxy population.

Our results provide fundamental, statistically robust observational constraints on the interplay between galactic feedback and the baryon cycle over 12 billion years of cosmic history. These measurements of outflow scaling relations, particularly in the previously unexplored high-redshift ($z > 3$), low-mass regime, will be crucial for calibrating the next generation of cosmological simulations and refining our theoretical understanding of galaxy evolution towards the Cosmic Dawn.

ACKNOWLEDGMENTS

EW thanks support of the National Science Foundation of China (Nos. 12473008). CL is supported by the Fundamental Research Funds for the Central Universities (WK2030250123). The authors gratefully acknowledge the support of Cyrus Chun Ying Tang Foundations.

The data products presented herein are retrieved from the Dawn JWST Archive (DJA). DJA is an initiative of the Cosmic Dawn Center (DAWN), which is funded by the Danish National Research Foundation under grant DNRF140.

APPENDIX

A. COMPARISON WITH EQUAL-WEIGHT STACKING

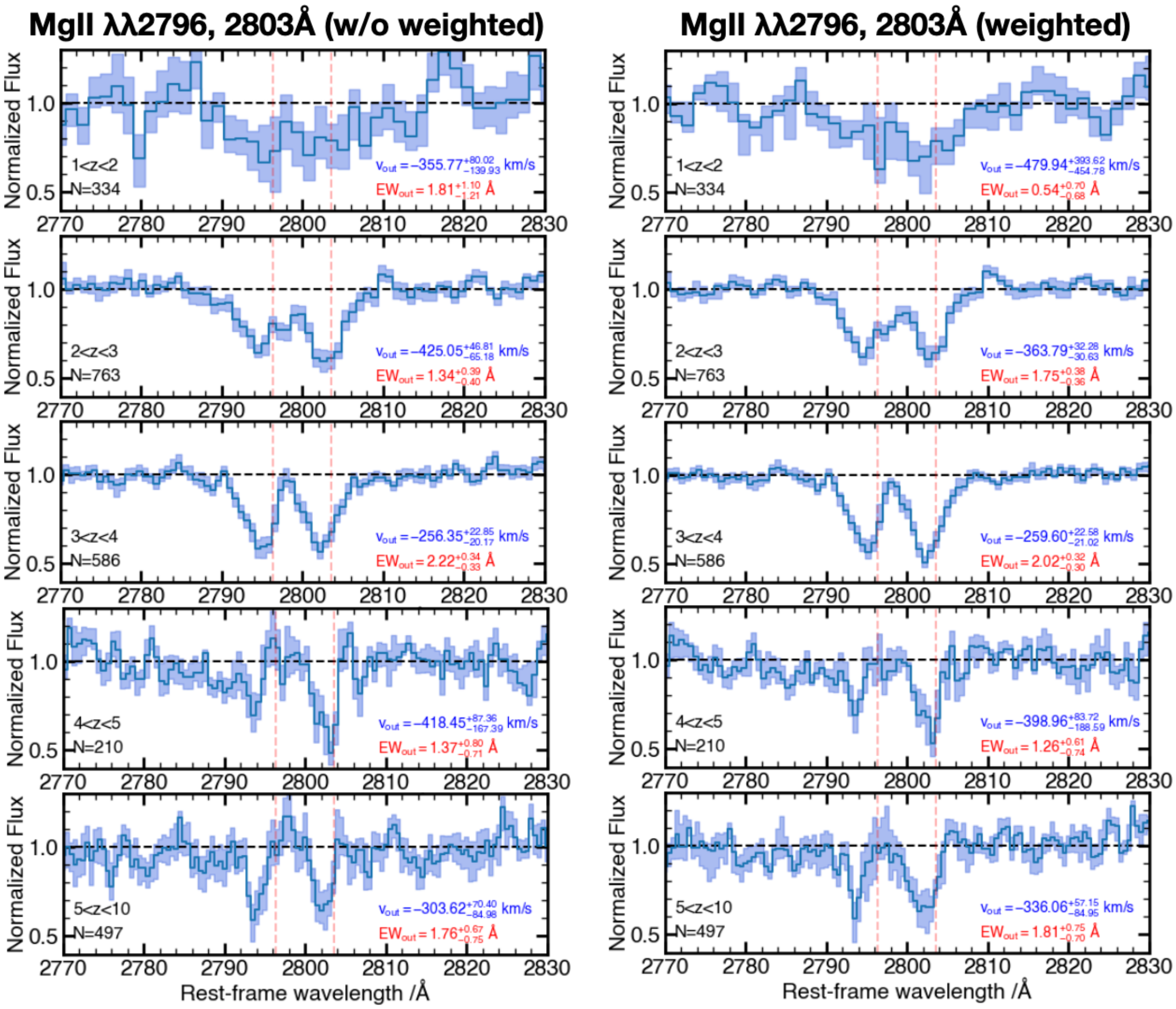

Figure 7. Comparison with equal-weight stacking. The left panels show the resulting stacked Mg II profiles for each redshift bin when using an unweighted (equal-weight) median stacking method. These profiles should be directly compared with the results from our fiducial S/N-weighted method (right panels, the same as in the left panels in Figure 2). Note the significantly lower S/N and less-defined absorption features compared to the weighted stacks, which demonstrates the superiority of the fiducial method.

In addition to the S/N-weighted stacking method adopted in our main analysis (Section 3), we perform a comparative test using an unweighted (equal-weight) stacking approach. In this alternative scheme, every spectrum contributes equally to the final stack, regardless of its individual S/N.

The left panels of Figure 7 presents the results of this test. A direct visual comparison with our fiducial stacks (right panels, the same as the left panels of Figure 2) immediately reveals the inferiority of this simpler method. Through involving poorly normalized individual spectra, composite spectra derived from unweighted stacking exhibits larger noise which is non-physical. This may potentially wash out the subtle, underlying absorption features. As a result, the continuum is more poorly defined, and the overall statistical significance of the detection is substantially lower. This comparison therefore underscores the critical importance of our S/N-weighting scheme for robustly detecting and characterizing the faint outflow signals in our sample. Although the effect of weighting is more subtle in our current, relatively small JWST sample, its importance becomes dramatic when stacking larger datasets to recover very faint signals.

B. INDIVIDUAL GALAXY SPECTRA OF ABSORBERS

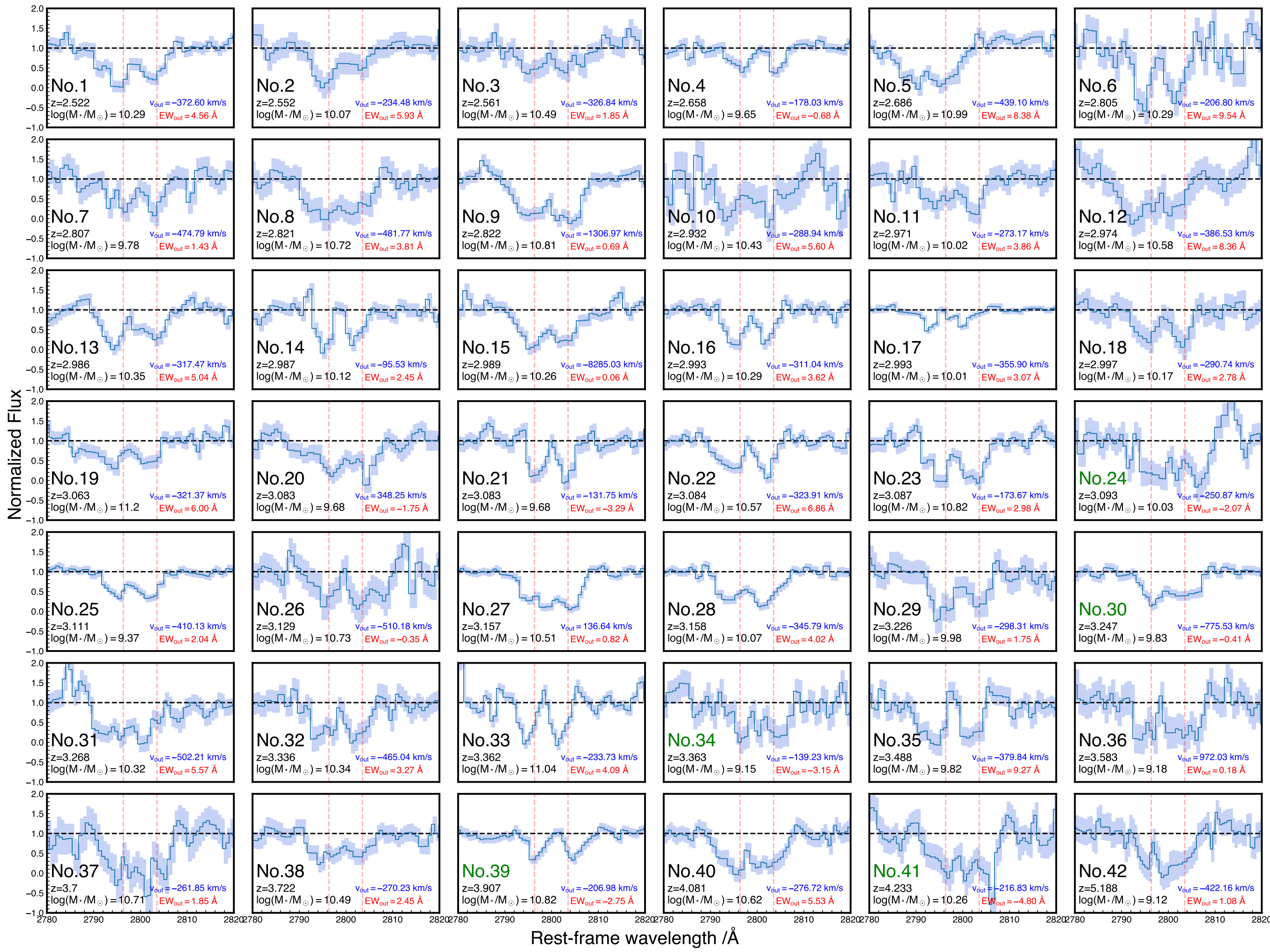

Figure 8. Individual Mg II absorption detections. Each panel shows the continuum-normalized spectrum of an individual galaxy from our sample, centered on the Mg II doublet region, with the panels arranged in order of increasing redshift. The shaded regions are 1σ uncertainties and the dashed lines mark the rest-frame Mg II doublet. Each spectrum is annotated with its spectroscopic redshift (z), stellar mass ($\log(M_*/\mathrm{M}_\odot)$), and the `boxcar`-measured velocity (v) and equivalent width (EW). While most objects show blueshifted absorption indicative of outflows, a few exhibit visually redshifted absorption (marked by green color), which may be a signature of gas inflow. These examples showcase the diversity of kinematics and data quality that contribute to our main stacking analysis.

While our main analysis relies on spectral stacking to overcome the low S/N inherent in most individual high-redshift spectra, a subset of galaxies in our sample do exhibit individually detectable Mg II absorption features. In Figure 8, we present a postage stamp gallery of such individual detections, selected to illustrate the presence of these features in our dataset. The corresponding properties of these individual galaxies and outflow measurements are tabulated in Table 2.

These examples highlight the significant kinematic diversity present in the underlying population. The majority of the selected objects display clear blueshifted absorption profiles (negative velocities), providing direct visual confirmation of the outflow signatures that

Table 2. Properties of Individual Galaxy with Mg II Absorption Detections. The columns are as follows: (1) Object number. (2) Object name in the DJA catalog. (3) Right Ascension. (4) Declination. (5) Spectroscopic redshift. (6) Logarithm of the stellar mass. (7) Mean outflow velocity derived from the Mg II doublet. (8) Outflow equivalent width of the Mg II doublet.

No.	Name in DJA catalog	R.A. (deg)	Dec. (deg)	$z_{\rm spec}$	$\log M_*$ ($M_\odot$)	$v_{\rm out}$ (km s^{-1})	EW$_{\rm out}$ (Å)
1	cosmos-curti-v4_g140m-f100lp_1879_3747	150.06155	2.23362	2.522	10.29	−372.60	4.56
2	bluejay-north-v4_g140m-f100lp_1810_16474	150.11344	2.34747	2.552	10.07	−234.48	5.93
3	bluejay-south-v4_g140m-f100lp_1810_8888	150.12873	2.26979	2.561	10.49	−326.84	1.85
4	cosmos-curti-v4_g140m-f100lp_1879_1858	150.08136	2.20749	2.658	9.65	−178.03	-0.68
5	bluejay-south-v4_g140m-f100lp_1810_8002	150.11993	2.26102	2.686	10.99	−439.10	8.38
6	jades-gds03-v4_g140m-f070lp_1286_181082	53.12218	−27.85834	2.805	10.29	−206.80	9.54
7	jades-gds1-v4_g140m-f070lp_1286_42789	53.18607	−27.80225	2.807	9.78	−474.79	1.43
8	gds-udeep-v4_g140m-f070lp_3215_199773	53.16324	−27.80906	2.821	10.72	−481.77	3.81
9	bluejay-north-v4_g140m-f100lp_1810_18071	150.13527	2.36361	2.822	10.81	−1306.97	0.69
10	jades-gdn2-v4_g140m-f070lp_1181_20185	189.10652	62.23063	2.932	10.43	−288.94	5.60
11	jades-gds04-v4_g140m-f070lp_1286_53237	53.04188	−27.86134	2.971	10.02	−273.17	3.86
12	jades-gdn10-v4_g140m-f070lp_1181_77071	189.22890	62.19548	2.974	10.58	−386.53	8.36
13	bluejay-north-v4_g140m-f100lp_1810_17793	150.13779	2.36100	2.986	10.35	−317.47	5.04
14	bluejay-north-v4_g140m-f100lp_1810_17906	150.12949	2.36170	2.987	10.12	−95.53	2.45
15	jades-gdn11-v4_g140m-f070lp_1181_25603	189.17021	62.23287	2.989	10.26	−8285.03	0.06
16	aurora-gdn02-v4_g140m-f100lp_1914_22384	189.16149	62.25202	2.993	10.29	−311.04	3.62
17	aurora-gdn02-v4_g140m-f100lp_1914_19848	189.16046	62.23943	2.993	10.01	−355.90	3.07
18	jades-gds-wide-v4_g140m-f070lp_1180_11929	53.13048	−27.77596	2.997	10.17	−290.74	2.78
19	jades-gds-wide3-v4_g140m-f070lp_1180_197911	53.16531	−27.81414	3.063	11.20	−321.37	6.00
20	gds-rieke-v4_g140m-f100lp_1207_54612	53.14468	−27.77118	3.083	9.68	348.25	-1.75
21	jades-gds1-v4_g140m-f070lp_1286_54612	53.14468	−27.77118	3.083	9.68	−131.75	-3.29
22	aurora-gdn01-v4_g140m-f100lp_1914_4113	150.13793	2.22025	3.084	10.57	−323.91	6.86
23	cosmos-curti-v4_g140m-f100lp_1879_599	150.09334	2.18999	3.087	10.82	−173.67	2.98
24	bluejay-south-v4_g140m-f100lp_1810_7934	150.09731	2.26012	3.093	10.03	−250.87	-2.07
25	aurora-gdn02-v4_g140m-f100lp_1914_21033	189.21160	62.24571	3.111	9.37	−410.13	2.04
26	jades-gdn11-v4_g140m-f070lp_1181_25351	189.17337	62.23041	3.129	10.73	−510.18	-0.35
27	aurora-gdn01-v4_g140m-f100lp_1914_4740	150.15878	2.22606	3.157	10.51	136.64	0.82
28	aurora-gdn01-v4_g140m-f100lp_1914_6143	150.18320	2.24024	3.158	10.07	−345.79	4.02
29	excels-uds04-v4_g140m-f100lp_3543_61762	34.27260	−5.22469	3.227	9.98	−298.31	1.75
30	aurora-gdn01-v4_g140m-f100lp_1914_8363	150.13641	2.26468	3.247	9.83	−775.53	-0.41
31	bluejay-south-v4_g140m-f100lp_1810_8338	150.07943	2.26452	3.268	10.32	−502.21	5.57
32	jades-gdn2-v4_g140m-f070lp_1181_2945	189.14089	62.28066	3.336	10.34	−465.04	3.27
33	aurora-gdn02-v4_g140m-f100lp_1914_11584	189.10502	62.28033	3.362	11.04	−233.73	4.09
34	aurora-gdn02-v4_g140m-f100lp_1914_23927	189.24105	62.25951	3.363	9.15	−139.23	-3.15
35	bluejay-south-v4_g140m-f100lp_1810_13297	150.11868	2.31445	3.488	9.82	−379.84	9.27
36	jades-gds03-v4_g140m-f070lp_1286_180657	53.11252	−27.85900	3.583	9.18	972.03	0.18
37	excels-uds04-v4_g140m-f100lp_3543_39063	34.29044	−5.26208	3.700	10.71	−261.85	1.85
38	excels-uds04-v4_g140m-f100lp_3543_56133	34.30228	−5.23394	3.722	10.49	−270.23	2.45
39	jades-gdn10-v4_g140m-f070lp_1181_82948	189.23303	62.23678	3.907	10.82	−206.98	-2.75
40	excels-uds02-v4_g140m-f100lp_3543_117004	34.28827	−5.13754	4.081	10.62	−276.72	5.53
41	excels-uds03-v4_g140m-f100lp_3543_45052	34.36713	−5.25202	4.233	10.26	−216.83	-4.80
42	aurora-gdn02-v4_g140m-f100lp_1914_100067	189.23479	62.25748	5.188	9.12	−422.16	1.08

NOTE—The outflow properties are measured using the `boxcar` method described in Section 3.

*In typical outflows, EW$_{\rm out} > 0$ or $v_{\rm out} < 0$. Any result with EW$_{\rm out} < 0$ or $v_{\rm out} > 0$ is purely numerical outputs (see Section 3).

our stacking method robustly recovers. However, the gallery also reveals more complex cases. A few systems (e.g., No.34, No.39, marked by green color) show visually net redshifted absorption, a potential signature of cool gas accreting onto the galaxy (inflow). A comprehensive analysis of these individual systems, including detailed spectral profile fitting to disentangle the complex interplay of outflows, inflows, and virial motions, is beyond the scope of this statistically-focused Letter. We will present such an analysis in a forthcoming paper.

Nevertheless, the clear presence of both dominant outflow signatures and more complex kinematic features underscores the dynamic nature of the CGM and validates our stacking approach for recovering the average, population-wide signal.

REFERENCES

Baron, D., Netzer, H., Davies, R. I., & Xavier Prochaska, J. 2020, MNRAS, 494, 5396, doi: 10.1093/mnras/staa1018

Belli, S., Park, M., Davies, R. L., et al. 2024, Nature, 630, 54, doi: 10.1038/s41586-024-07412-1

Bergeron, J., & Stasińska, G. 1986, A&A, 169, 1

Bordoloi, R., Lilly, S. J., Kacprzak, G. G., & Churchill, C. W. 2014, ApJ, 784, 108, doi: 10.1088/0004-637X/784/2/108

Brammer, G. 2022, gbrammer/msaexp: Full working version with 2d drizzling and extraction, 0.3 Zenodo, doi: 10.5281/zenodo.7299501

Brammer, G. 2023, grizli, 1.9.11 Zenodo, doi: 10.5281/zenodo.8370018

Carnall, A. C. 2017, arXiv e-prints, arXiv:1705.05165, doi: 10.48550/arXiv.1705.05165

Chabrier, G. 2003, PASP, 115, 763, doi: 10.1086/376392

Chen, Y.-M., Tremonti, C. A., Heckman, T. M., et al. 2010, AJ, 140, 445, doi: 10.1088/0004-6256/140/2/445

Chen, Z., Wang, E., Zou, H., et al. 2025a, ApJ, 981, 81, doi: 10.3847/1538-4357/ada942

Chen, Z., Wang, E., Zou, H., et al. 2025b, ApJL, 988, L39, doi: 10.3847/2041-8213/ade545

Churchill, C. W., Mellon, R. R., Charlton, J. C., et al. 2000, ApJ, 543, 577, doi: 10.1086/317120

Clarke, L., Shapley, A. E., Lam, N., et al. 2025, arXiv e-prints, arXiv:2510.06681, doi: 10.48550/arXiv.2510.06681

Cresci, G., Tozzi, G., Perna, M., et al. 2023, A&A, 672, A128, doi: 10.1051/0004-6361/202346001

Croton, D. J., Springel, V., White, S. D. M., et al. 2006, MNRAS, 365, 11, doi: 10.1111/j.1365-2966.2005.09675.x

Davies, R. L., Belli, S., Park, M., et al. 2024, MNRAS, 528, 4976, doi: 10.1093/mnras/stae327

Davis, J. D., Tremonti, C. A., Swiggum, C. N., et al. 2023, ApJ, 951, 105, doi: 10.3847/1538-4357/accbbf

de Graaff, A., Brammer, G., Weibel, A., et al. 2025, A&A, 697, A189, doi: 10.1051/0004-6361/202452186

Dekel, A., Sarkar, K. C., Birnboim, Y., Mandelker, N., & Li, Z. 2023, MNRAS, 523, 3201, doi: 10.1093/mnras/stad1557

Di Matteo, T., Springel, V., & Hernquist, L. 2005, Nature, 433, 604, doi: 10.1038/nature03335

Erb, D. K. 2015, Nature, 523, 169, doi: 10.1038/nature14454

Finlator, K., & Davé, R. 2008, MNRAS, 385, 2181, doi: 10.1111/j.1365-2966.2008.12991.x

Förster Schreiber, N. M., Übler, H., Davies, R. L., et al. 2019, ApJ, 875, 21, doi: 10.3847/1538-4357/ab0ca2

Gardner, J. P., Mather, J. C., Clampin, M., et al. 2006, SSRv, 123, 485, doi: 10.1007/s11214-006-8315-7

Heckman, T. M., Lehnert, M. D., Strickland, D. K., & Armus, L. 2000, ApJS, 129, 493, doi: 10.1086/313421

Heintz, K. E., Brammer, G. B., Watson, D., et al. 2025, A&A, 693, A60, doi: 10.1051/0004-6361/202450243

Hopkins, P. F., Hernquist, L., Cox, T. J., & Kereš, D. 2008, ApJS, 175, 356, doi: 10.1086/524362

Kehoe, E., Shapley, A. E., Sanders, R. L., et al. 2025, arXiv e-prints, arXiv:2506.17381, doi: 10.48550/arXiv.2506.17381

Li, Z., Dekel, A., Sarkar, K. C., et al. 2024, A&A, 690, A108, doi: 10.1051/0004-6361/202348727

Liboni, C., Belli, S., Bugiani, L., et al. 2025, arXiv e-prints, arXiv:2506.05470, doi: 10.48550/arXiv.2506.05470

Looser, T. J., D'Eugenio, F., Maiolino, R., et al. 2025, A&A, 697, A88, doi: 10.1051/0004-6361/202347102

Lyu, C., Wang, E., Zhang, H., et al. 2025a, ApJL, 981, L6, doi: 10.3847/2041-8213/adb4ed

Lyu, C., Wang, E., Wang, J., et al. 2025b, ApJL, 988, L72, doi: 10.3847/2041-8213/adf0f9

Martin, C. L., Shapley, A. E., Coil, A. L., et al. 2012, ApJ, 760, 127, doi: 10.1088/0004-637X/760/2/127

Pettini, M., Shapley, A. E., Steidel, C. C., et al. 2001, ApJ, 554, 981, doi: 10.1086/321403

Pollock, C. L., Gottumukkala, R., Heintz, K. E., et al. 2025, arXiv e-prints, arXiv:2506.15779, doi: 10.48550/arXiv.2506.15779

Rubin, K. H. R., Prochaska, J. X., Koo, D. C., et al. 2014, ApJ, 794, 156, doi: 10.1088/0004-637X/794/2/156

Rubin, K. H. R., Weiner, B. J., Koo, D. C., et al. 2010, ApJ, 719, 1503, doi: 10.1088/0004-637X/719/2/1503

Rupke, D. S., Veilleux, S., & Sanders, D. B. 2005, ApJS, 160, 115, doi: 10.1086/432889

Savage, B. D., & Sembach, K. R. 1996, ARA&A, 34, 279, doi: 10.1146/annurev.astro.34.1.279

Silk, J., & Rees, M. J. 1998, A&A, 331, L1, doi: 10.48550/arXiv.astro-ph/9801013

Somerville, R. S., Hopkins, P. F., Cox, T. J., Robertson, B. E., & Hernquist, L. 2008, MNRAS, 391, 481, doi: 10.1111/j.1365-2966.2008.13805.x

Tremonti, C. A., Heckman, T. M., Kauffmann, G., et al. 2004, ApJ, 613, 898, doi: 10.1086/423264

Tumlinson, J., Peeples, M. S., & Werk, J. K. 2017, ARA&A, 55, 389, doi: 10.1146/annurev-astro-091916-055240

Valentino, F., Heintz, K. E., Brammer, G., et al. 2025, A&A, 699, A358, doi: 10.1051/0004-6361/202553908

Veilleux, S., Cecil, G., & Bland-Hawthorn, J. 2005, ARA&A, 43, 769, doi: 10.1146/annurev.astro.43.072103.150610

Veilleux, S., Maiolino, R., Bolatto, A. D., & Aalto, S. 2020, A&A Rv, 28, 2, doi: 10.1007/s00159-019-0121-9

Wang, E., & Lilly, S. J. 2021, ApJ, 910, 137, doi: 10.3847/1538-4357/abe413

Weaver, J. R., Davidzon, I., Toft, S., et al. 2023, A&A, 677, A184, doi: 10.1051/0004-6361/202245581

Weiner, B. J., Coil, A. L., Prochaska, J. X., et al. 2009, ApJ, 692, 187, doi: 10.1088/0004-637X/692/1/187

Yu, H., Wang, E., & Chen, Z. in prep.,